AIAA JOURNAL
Vol. 42, No. 4, April 2004

Study of Vortical Separation from Three-Dimensional Symmetric Bumps

Gwibo Byun,* Roger L. Simpson,† and C. H. Long‡
Virginia Polytechnic Institute and State University, Blacksburg, Virginia 24061

Surface mean pressures, oilflow visualization, and three-velocity-component laser Doppler velocimeter (LDV) measurements are presented for a turbulent boundary layer of momentum thickness Reynolds number, $Re_\theta \approx 7300$, and of thickness δ over two axisymmetric bumps of height $H = \delta$ and 2δ and one symmetric bump of $H = 2\delta$. LDV data were obtained at one plane, $x/H \geq 3.26$, for each case. Complex vortical separations occur on the lee side and merge into large streamwise mean vortices downstream for the two axisymmetric cases. The near-wall flow ($y^+ < 90$) is dominated by the wall. For the axisymmetric cases, the vortices in the outer region produce large turbulence levels near the centerline and appear to have low-frequency motions that contribute to turbulent diffusion. For the case with a narrower spanwise shape, there are sharper separation lines and lower turbulence intensities in the vortical downstream flow.

Introduction

THERE have been a few previous studies of boundary-layer flow over a symmetric hill, although little has been reported about the near-wall and separated vortical flows in references cited by Ishihara et al.[1] Ishihara et al. examined the flow in the center plane of an axisymmetric hill that had a cosine-squared cross section and a maximum slope of 32 deg. The approach boundary-layer thickness to hill height ratio (δ/H) was 9 and the Reynolds number $U_H H/\upsilon = 1.1 \times 10^4$, where U_H is the velocity at height H for the undisturbed boundary layer. Although little was presented about the flow away from the center plane, it was clear that the flow accelerated over the top and around the sides of the hill. A lee-side separation and a reattachment at the foot of the hill occurred with low-frequency motions ($0.065 < fH/U_H < 0.13$) in the downstream wall layer at $x/H = 3.75$.

Some objectives of the current research program are to measure and understand the formation and structure of vortical three-dimensional turbulent separations of a turbulent boundary layer over symmetric hills or bumps, which are used to create strong streamwise vortices that energize the downstream boundary layer. Of particular interest are data that describe the turbulent diffusion processes that control the momentum transfer rates that affect the vortical separation. Another objective is to provide test cases to compare with and modify turbulence models that are used to calculate such flows. Symmetric hills were selected that have multiple separations over a large area of the lee side. Such flows are more demanding of turbulence models than attached or massively separated flow cases. Three bumps, two axisymmetric bumps of height $H = \delta$, 2δ and one symmetric bump of $H = 2\delta$, were considered in this paper.

To understand the nearest wall flow where the separations originate, detailed surface pressure distributions and surface oil-flow patterns were obtained. Precise very-near-wall measurements of mean velocities, turbulent stresses, triple products, and skin friction have been obtained (Fig. 1). Simpson et al.[2] discussed the oil flow, surface pressures, and vorticity flux and the wake plane results for the large bump 3 shown in Fig. 2.

Experimental Apparatus and Flow Conditions

The measurements were conducted in the Virginia Polytechnic and State University Aerospace and Ocean Engineering Department low-speed boundary-layer wind tunnel, which has been used much in previous work and is described by Devenport and Simpson.[3] At a nominal speed of $U_{\text{ref}} = 27.5$ m/s and temperature of 25 ± 1°C, the turbulence intensity observed in the tunnel freestream was 0.1% and the potential core was uniform to within 0.5% in the spanwise and 1% in the vertical directions. When a given bump was not in place, a mean two-dimensional zero pressure gradient turbulent boundary layer 39 mm thick was present with $Re_\theta = 7300$, the same conditions reported by Ölçmen and Simpson.[4] Each bump was mounted in the center floor of the 0.91-m-wide, 0.25-m-high, and 7.62-m-long test section 2.9 m from the test section leading edge. Each bump 3 was machined with the axisymmetric shape shown in Fig. 3, which is defined by

$$y(r)/H = -(1/6.04844)\{J_0(\Lambda)I_0[\Lambda(r/a)] - I_0(\Lambda)J_0[\Lambda(r/a)]\} \tag{1}$$

where $\Lambda = 3.1962$. For large bump 3, $H = 78$ mm is the height of the bump; for small bump 3, $H = 39$ mm. For both bumps 3, $a = 2H$ is the radius of the circular base of the bump, J_0 is the Bessel function of the first kind, and I_0 is modified Bessel function of the first kind.

Bump 1 has the same streamwise shape and height as large bump 3, but with a narrower symmetric shape in the spanwise direction defined by

$$\begin{aligned} y(x,z)/H = {} & (1/1.1329^2)\{\cos[4.73(x/a)] \\ & + 0.1329\cosh[4.73(x/a)]\}\{\cos[4.73(z/b)] \\ & + 0.1329\cosh[4.73(z/b)]\} \end{aligned} \tag{2}$$

Bump 1 has a rectangular base with length $a = 4H$ and width $b = 2H$. Figure 3 shows the three-dimensional shapes of bump 3 and bump 1 normalized by the bump height H. The Reynolds number based on the height H and U_{ref} is $Re_H \approx 1.3 \times 10^5$ for the two larger bumps.

Laser-Doppler System

Two configurations of a three-velocity-component fiber-optic laser Doppler velocimetry (LDV) system were used to obtain coincident instantaneous U, V, and W components of the velocity through

Presented as Paper 2003-0641 at the AIAA 41st Aerospace Sciences Meeting, Reno, NV, 6–9 January 2003; received 9 April 2003; accepted for publication 17 December 2003.

*Graduate Research Assistant, Department of Aerospace and Ocean Engineering. Student Member AIAA.
†Jack E. Cowling Professor, Department of Aerospace and Ocean Engineering. Fellow AIAA.
‡Graduate Research Assistant, Department of Aerospace and Ocean Engineering.

the transparent glass test wall. In the nearer wall "short" LDV configuration (Fig. 4), which is well described by Ölçmen and Simpson[5] including velocity measurement uncertainties, measurements can be made within 40 mm of the surface; the effective measurement volume of approximately 30 μm in diameter permits precise near-wall (about $y^+ = 3$) measurements. In the outer-layer "long" LDV configuration (Fig. 4), which is well described by Ölçmen et al.[6] along with velocity measurement uncertainties, measurements can be made within 160 mm of the surface with a reduced spatial resolution of 88 μm, which is of no consequence for outer-layer spatial resolution. The data validation percentage from the Macrodyne

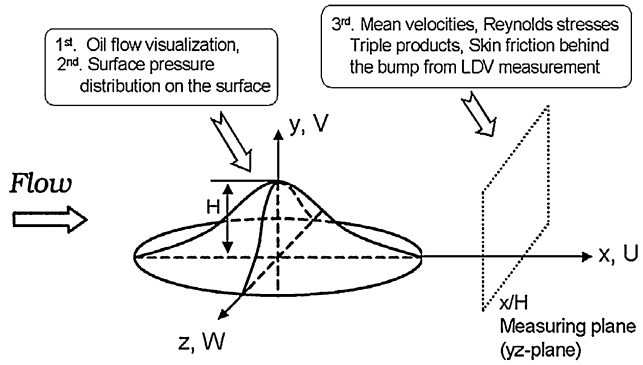

Fig. 1 Schematic showing types of measurements.

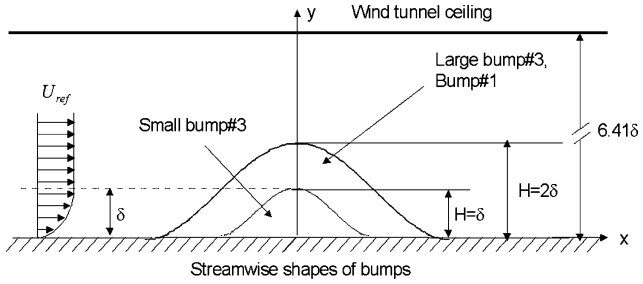

Fig. 2 Axisymmetric shapes of bump 3 and the streamwise shape of bump 1.

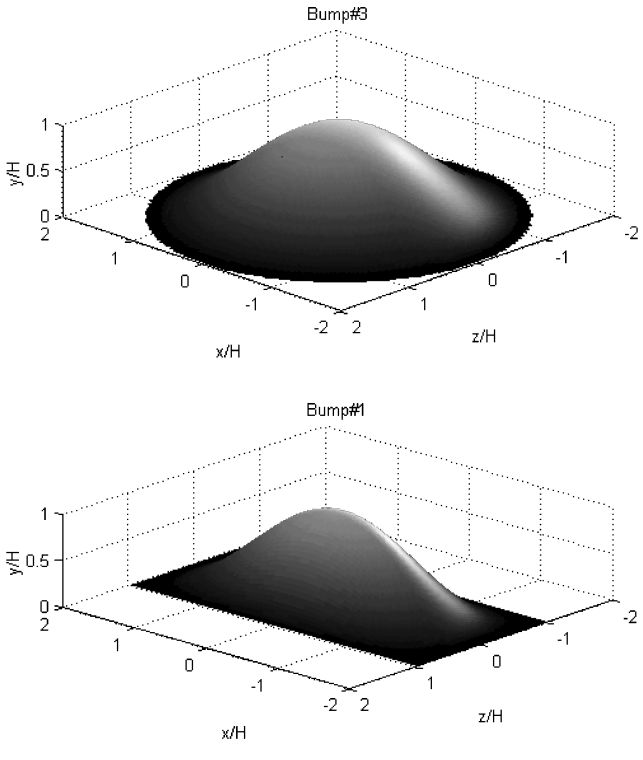

Fig. 3 Three-dimensional shapes of bumps.

model 3100 frequency domain processors was above 98%, which resulted in minimally noisy data. One block of 30,000 samples was taken over several minutes for each measurement point. The aerosol seeding system[5] used dioctal phthalate with a measured mean particle size of about 2 μm. The outlying data points from histograms were removed in the LDV optics coordinate system as well as after rotation into the tunnel coordinate system, as described by Ölçmen and Simpson.[5] Because there was no correlation between the data rate fluctuation and the velocity magnitude fluctuation, no velocity bias correction was applied. Velocity gradient, finite transit time, and instrument broadening of the signals were also negligible. The data shown here are composite data from the two LDV configurations.

Surface Static Pressure Coefficient and Vorticity Flux

Mean static pressure distributions were measured on the surface of each bump and on the plate upstream and downstream by using multiple pressure taps flush with the surface that are connected to a Scani valve system. The static pressure coefficient C_p is calculated as

$$C_P = \frac{P_{\text{local,static}} - P_{\text{ref,static}}}{P_{\text{ref,total}} - P_{\text{ref,static}}} \tag{3}$$

where $p_{\text{ref,static}}$ and $p_{\text{ref,total}}$ are the static and stagnation pressures of the undisturbed freestream that determine U_{ref} and are measured by a pitot static tube mounted 1.4 m upstream of the center of the bump, where $x = 0$. The 0.5-mm-diam pressure taps were placed along a radial line of the bump, 6.35 mm apart. For the axisymmetric bumps, the pressure measurements were made every 10 deg of peripheral angle by turning the bump around the y axis of symmetry. Three dozen pressure taps were placed on the flat Plexiglas® plate. These pressure taps were only at one side of the centerline, because the flow over the plate is symmetric about the centerline as verified by the pressure data on the bump. Also the taps on the plates were only placed at one side of the bump (upstream or downstream), but the pressure data were taken for both upstream and downstream by turning the plates with the bump 180 deg. The contour plot of surface static pressure coefficient C_p (± 0.02 uncertain) shown in Fig. 5 is only for large and small bump 3, which uses data from both sides of the plane of symmetry. Differences in C_p are generally less than ± 0.02 from an average for any two symmetric locations and show good symmetry. Because the only pressure data for bump 1 are along the centerline, there is no contour plot of bump 1. However, C_p distributions along the centerline of bump 1 are compared with Applied Research Laboratory (ARL) experimental and computational data.[7] For the region upstream of the bump, present data agree well with q–ω model results. This model has been observed to calculate two-dimensional separating flows better than some other models.[8] Data show higher C_p than computational results, but still agree with ARL experimental results. It is noted that at the downstream region, C_p recovers from the minimum value at the top of the bump ($x/H = 0$) to its maximum value at the edge of the bump ($x/H = 2$), which is even higher than the highest upstream value ($x/H = -1.6$). This is probably due to the strongly decelerated flow without a strong separation in that region.

For incompressible flow over stationary surfaces with a unit vector normal to the surface $\boldsymbol{e}_n$, all vorticity, $\boldsymbol{\omega} = \text{curl}\boldsymbol{V}$, arises at the surface under the action of pressure gradients. The flux of vorticity at the surface is directly proportional to and perpendicular to the pressure gradient at the surface:

$$\frac{4}{Re_H}\left[\frac{\partial(\omega H/U_{\text{ref}})}{\partial(n/H)}\right]_W = -(\boldsymbol{e}_n \times \boldsymbol{\nabla})C_P \tag{4}$$

The vector plots of $-(\boldsymbol{e}_n \times \boldsymbol{\nabla})C_P$, the nondimensional vorticity flux, are presented in Fig. 6. The vortex filaments are created in closed loops, which coincide with isobars in Fig. 5. The fresh vorticity on the upstream side of the bump is of the same sign as the approach boundary-layer vorticity and it is strongly generated at the top of the bumps. On the sides of the bump the new vorticity is mainly in the streamwise, but opposite, directions. Downstream of the bump top, the fresh vorticity is opposite that of the approach boundary layer. The nonuniform generation of vorticity

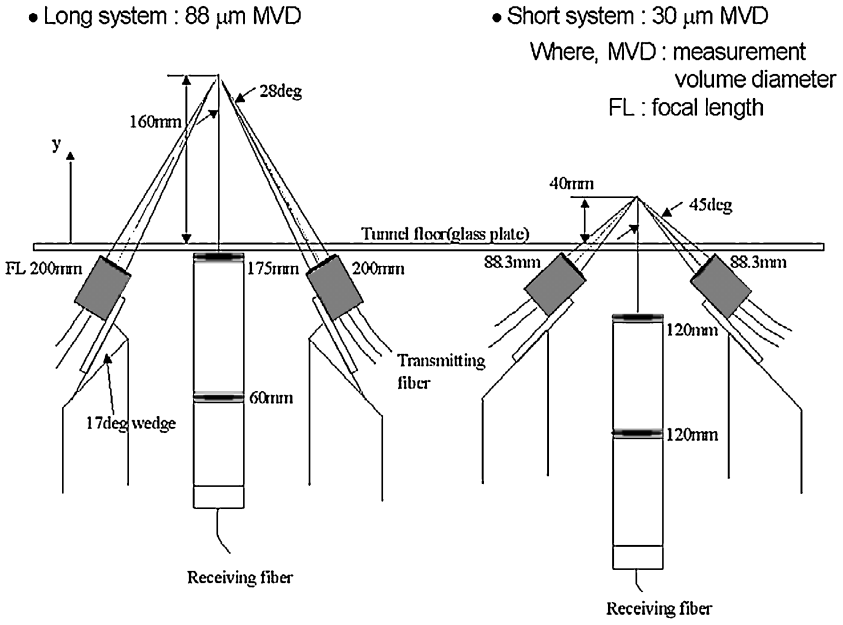

Fig. 4 Schematic diagram of the 2 LDV configurations.

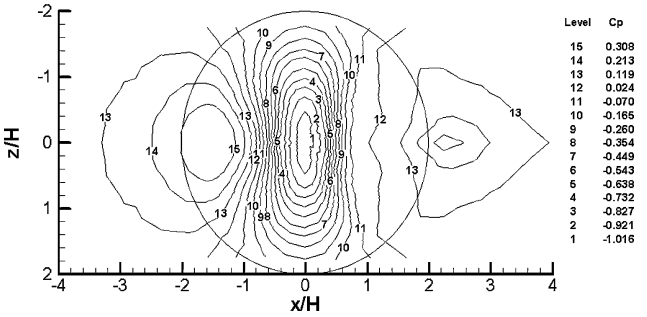

a) Large bump 3

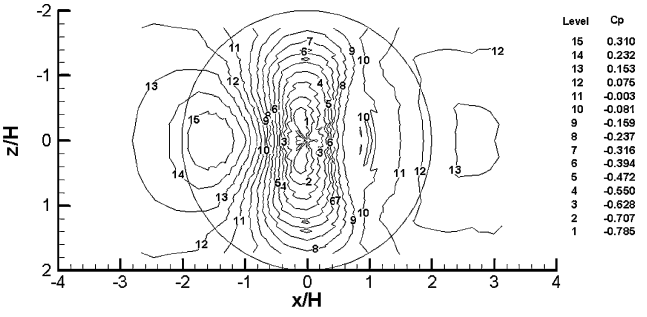

b) Small bump 3

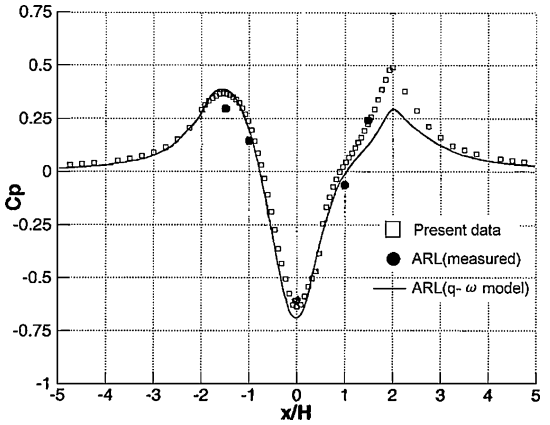

c) Bump 1 along the centerline: present and ARL data[7]

Fig. 5 Pressure coefficient of the bumps.

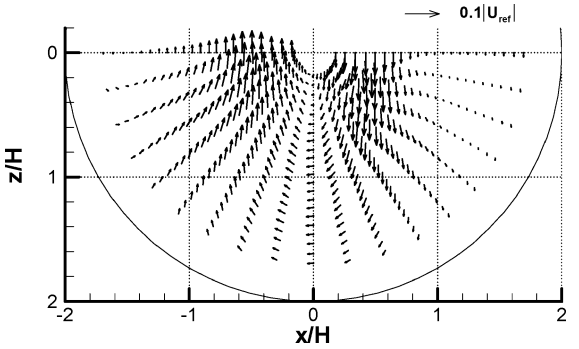

a) Large bump 3

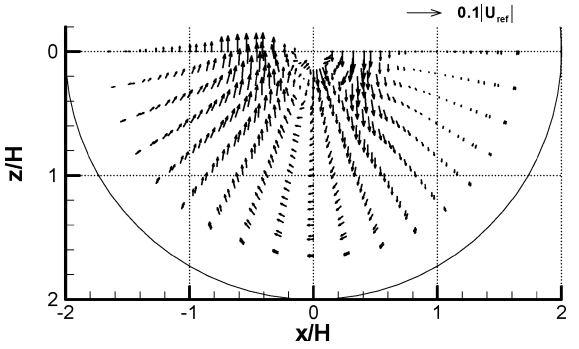

b) Small bump 3

Fig. 6 Vector plot of nondimensional vorticity flux at the surface of the bumps.

across the flow and the rate of diffusion of vorticity control the three-dimensional separation patterns.

Surface Oilflow Visualization

Surface oilflow visualization of skin friction lines, high- and low-velocity regions, separations, and reattachments were obtained for the bumps and the tunnel floor. The oil mixture was 20% oleic acid, 20% titanium dioxide, and 60% kerosene. The surfaces of the black model and the Plexiglas plate that was covered with self-adhesive black plastic film were coated uniformly with a layer of the oil mixture. The tunnel was turned on as soon as the oil mixture was applied and was kept running until the flow moved the oil into a consistent

and partially dry streak. The streaks form wall shear stress lines, that is, a limiting streamline pattern. The patterns were photographed, examined, and preserved by clear acrylic spray lacquer.

The oilflow patterns photographed during the flows (Figs. 7–9) were not definitive in the strong separation region on the lee side of bumps 3 because excessive oil mixture accumulated where the shear-stress lines spiraled into foci and tended to flow down the bump due to gravity. Videos were made to observe movement of the oil mixture; static pictures were made from the video for further quantitative analysis. Also, small drops of the oil mixture were placed on the lee side of a clean bump and video was taken. This helped to determine definitively the direction of oilflow movement. The resulting oilflow shear-stress line pattern was interpreted according to the kinematical topological rules described by Hunt et al.[9] and is shown in Figs. 7–9.

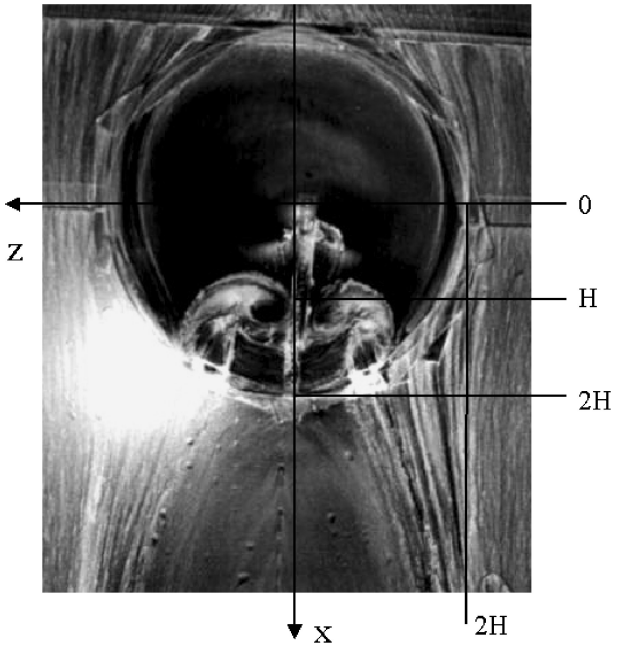

a) Top view of an oil flow

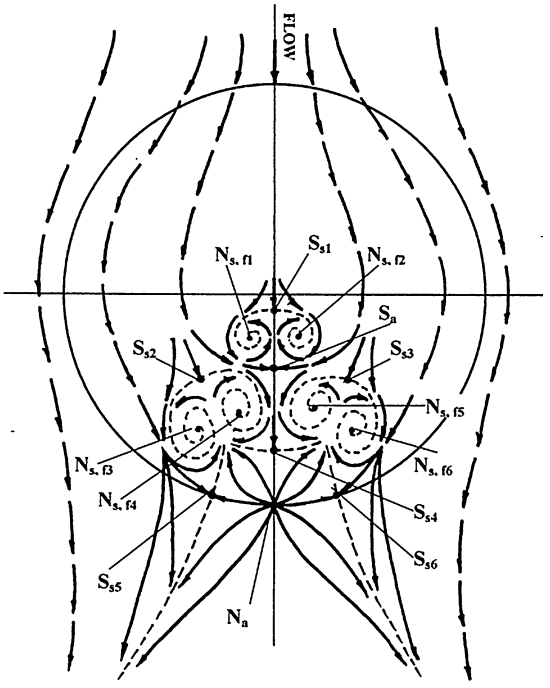

b) Shear stress lines (bold), separation lines (dashed), and zero shear stress points on the surface

Fig. 7 Oilflow visualization results for large bump 3.

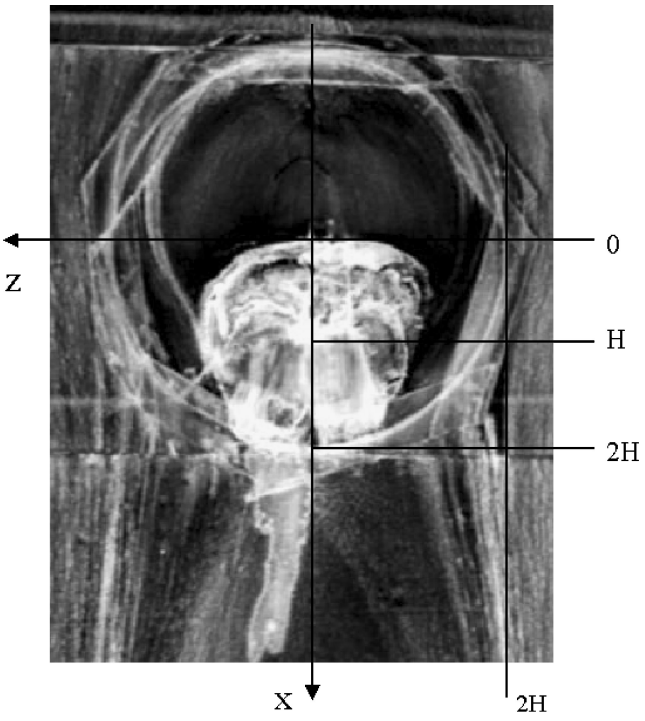

a) Top view of an oil flow

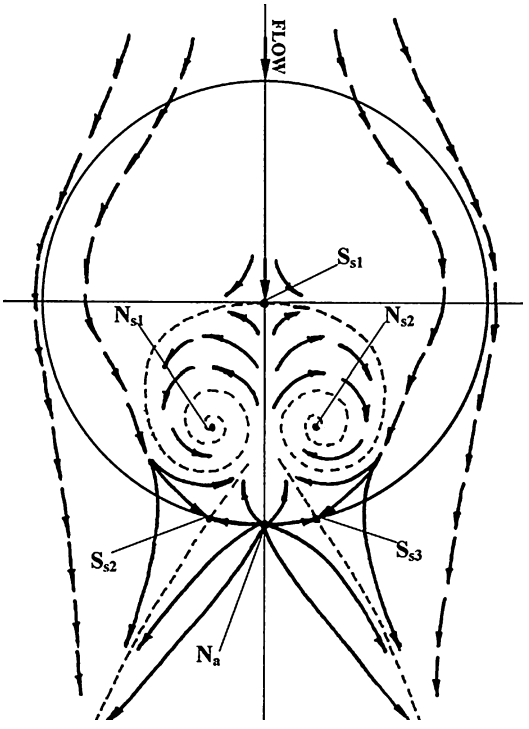

b) Shear stress lines (bold), separation lines (dashed), and zero shear stress points on the surface

Fig. 8 Oilflow visualization results for small bump 3.

Discussion of Oilflow Visualization and Surface Static Pressure Distribution

There is no separation on the front of each bump, but the flow decelerates and oil flow accumulates there. Then the flow accelerates until the top of the bump, where the oil flow is dark because the shearing stress is large and there is little oil mixture left.

Figure 7 shows the oilflow results of large bump 3. Downstream on the lee side there is a region with much accumulated oilflow mixture, approximately from $x/H = 0.18$ to 0.4 and from $z/H = \pm 0.35$. From the shear stress lines in Fig. 7, there is one saddle separation

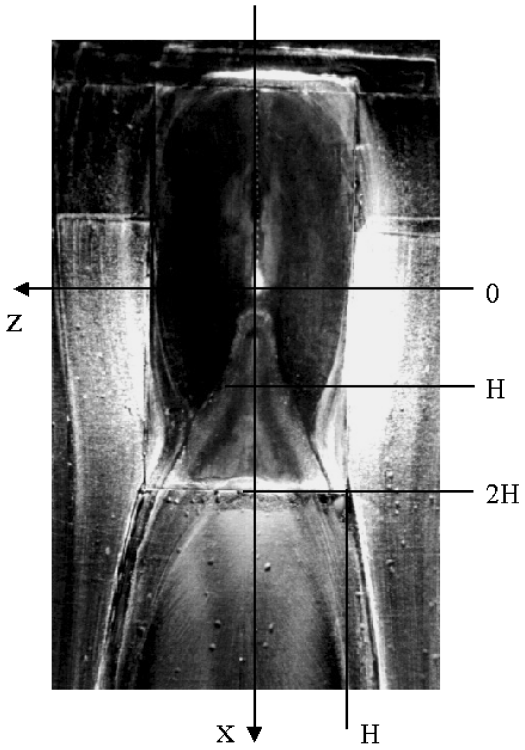

a) Top view of an oil flow

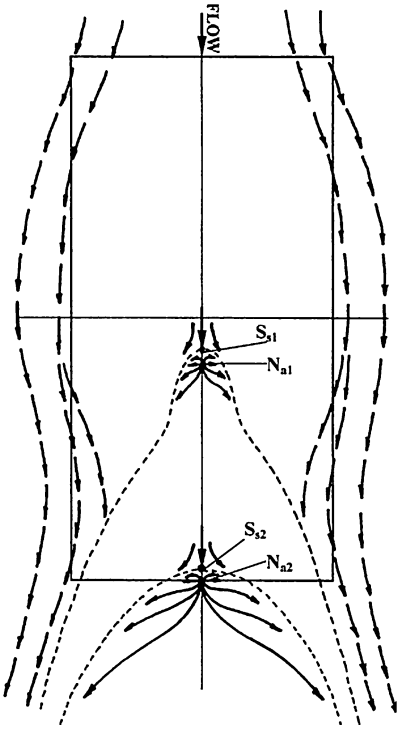

b) Shear stress lines (bold), separation lines (dashed), and zero shear stress points on the surface

Fig. 9 Oilflow visualization results for bump 1.

S_{s1} on the x axis, followed by symmetrical foci node separations $N_{s,\text{focus1}}$ and $N_{s,\text{focus2}}$ on each side of the centerline. Just downstream a saddle attachment S_a occurs, around which the oil flow is darker because of higher shearing stresses. From the C_p (Fig. 5) and pressure gradient distributions, we can see that this area is also followed by a region from $x = 0.4H$ to $0.5H$ with very high adverse pressure gradients. A large separation appears to begin from this region with a relaxation of the downstream pressure gradients. After $x/H = 0.8$, between ± 30 deg of the centerline, the pressure only increases slightly. Saddle separations S_{s2} and S_{s3} occur symmetrically near $x = 0.8H$ and $z = \pm 0.7H$. Foci separations $N_{s,\text{focus3}}$ and $N_{s,\text{focus4}}$ are downstream of S_{s2}, and $N_{s,\text{focus5}}$ and $N_{s,\text{focus6}}$ are downstream of S_{s3}; each is about $0.4H$ in diameter. Slightly downstream at about $x = 1.5H$ on the centerline, another saddle separation S_{s4} is located with a distinctly greater accumulation of oilflow mixture upstream. At the bottom of the bump near $x = 2H$, a nodal attachment N_a occurs, which supplies higher speed fluid in all directions and produces a darker oil flow. Saddle separations S_{s5} and S_{s6} are located on each side of the bottom of the bump at about $z = \pm 0.7H$. Separation lines that pass through S_{s5} and S_{s6} continue downstream and form a line between the higher velocity flow near the centerline and the lower speed flow. The number of saddles and nodes satisfying the topological rule, $\Sigma N = \Sigma S$, is seven.

Figure 8 shows the oilflow results of small bump 3. Because the oilflow results were not preserved well after the tunnel stopped running, the analysis was done by videos and small drops, as mentioned earlier, as well as by photographs. The flow in the plane of symmetry separates near the top of the bump as indicated by the oil mixture accumulation. This area is followed by a high adverse pressure gradient region (see C_p in Fig. 5). The lateral flow separates at the bottom of the bump. There are saddle separations S_{s2} and S_{s3} at about $x/H = 2$ and $z/H = 0.4$ on each side. Also at the bottom of the bump, near $x = 2H$, the separated flow attaches at nodal attachment N_a on the centerline. The backflow from the separation, together with the flow coming around the bump, forms a pair of foci node separations $N_{S1,\text{focus}}$ and $N_{S2,\text{focus}}$ at about $x/H = 0.8$ and $z/H = 0.4$. Unlike large bump 3, small bump 3 shows only one strong separation at the top and one attachment at the bottom of the bump. Also there is only one pair of foci node separations. The number of saddles and nodes satisfy the topological rule: $\Sigma N = \Sigma S = 3$.

Figure 9 shows the oilflow results of bump 1. There is no oil mixture accumulation like that for bumps 3. Downstream right after the top of the bump, however, we can see the sharp separation line like an upside-down V. It is followed by a dark region. This means that, just after the saddle separation S_{S1} at around $x/H = 0.2$, the separated flow attaches at node attachment N_{a1}. Another separation line is observed from about $x/H = 1.9$ to the downstream tunnel floor, and so there is another pair of saddle separation S_{S2} and node attachment N_{a2}. The difference between bump 1 and bump 3 is that there is no foci separation. Bump 1 also satisfies the topological rules: $\Sigma N = \Sigma S = 2$.

Laser-Doppler Velocimetry Results

The LDV results for the undisturbed two-dimensional turbulent boundary layer agreed with previous data and the nearest wall triple products agreed with low-Reynolds-number direct numerical simulation results.[10] All data satisfy the realizability conditions[11] too. The LDV results presented here for the bumps were obtained in a y–z plane located downstream from the top of the bumps ($x/H = 3.63$ for large bump 3, $x/H = 3.26$ for small bump 3, and $x/H = 3.46$ for bump 1) with profiles for $-2.85 \le z/H \le 0.81$. Note that "two-dimensional flow" profiles were measured at $x/H = 0$ for large bump 3 without the bump.

The uncertainty was calculated using two acquired data sets and Chauvenet's criterion to calculate the standard deviation σ:

$$d_{\max}/\sigma = 1.15 \tag{5}$$

where $d_{\max}$ is the average of half of the differences between two data values; 21-to-1 odds uncertainties were calculated as $\pm 2\sigma$ in Table 1.

Skin Friction Results

Figure 10 shows the magnitude of U_τ/U_{ref}($\pm 5\%$ uncertainty) that was determined by the viscous sublayer data. As described by Long,[10] when the measurement volume was focused just on the surface, a strong signal determined an approximate reference location for an LDV traverse. A more refined determination of the measurement volume location relative to the wall was obtained by a least-squares curve fit of the viscous sublayer mean velocity profile,

$Q = C_1 y + C_2 y^4$ (Ref. 12), where $Q = (\bar{U}^2 + \bar{W}^2)^{1/2}$ and C_1 and C_2 are coefficients. The curve was fit through $Q = 0$ at $y = 0$. Using only the data for $y^+ < 10$, an iterative process was used to maximize the curve-fit correlation coefficient by shifting the y values by Δy. This was performed at each of the profiles using at least four points. Most of the optimum Δy shifts were less than 50 μm. Using this curve fit, the wall shearing stress $\tau_w/\rho = \upsilon(\partial Q/\partial y)_{\text{wall}} = U_\tau^2 = C_1\upsilon$, where υ is the kinematic viscosity. The product moment of correlation coefficient, R_c, between the data and the curve fit was $R_c > 0.995$ for all z/H.

The effect of pressure gradient on U_τ was considered, too. Thus, the model equation would be $Q = C_1 y + C_2 y^2 + C_3 y^4$, in which $C_2 = (\boldsymbol{n}_Q \cdot \boldsymbol{\nabla} P)/2\mu$ was determined by the magnitude of the pressure gradient in the Q direction.[12] The $\boldsymbol{n}_Q$ is the unit vector in the Q direction and μ is the viscosity. Unfortunately, no pressure data were available at each LDV measurement location except the centerline ($z/H = 0$). The nearest upstream pressure data from the LDV measurement location were used for curve fitting of off-center points as mentioned earlier ($x/H = 2.75$ for $z/H = \pm 0.49$ and $x/H = 2.5$ for $z/H = -0.98, -1.47$). Although these pressure data were not measured at the location where LDV data were taken and these pressure gradients are larger than those downstream, it is possible to estimate how much the pressure gradient affects $|U_\tau|$; $|U_\tau|$ was changed less than 1.5% by the pressure gradient. However, the product moment of correlation coefficient between the data and the curve fit was $R_c > 0.999$ for all stations that were calculated. This indicates a better fit than when the pressure gradient was not considered. It increased around the center due to a favorable pressure gradient and decreased away from the center because of an adverse pressure gradient.

Table 1 Uncertainties in measured quantities in 21:1 odds

Quantity	Uncertainty
$\bar{U}/U_{\text{ref}}$	±0.0026
$\bar{V}/U_{\text{ref}}$	±0.0014
$\bar{W}/U_{\text{ref}}$	±0.0025
$\overline{u^2}/U_{\text{ref}}^2$	±0.00024
$\overline{v^2}/U_{\text{ref}}^2$	±0.00011
$\overline{w^2}/U_{\text{ref}}^2$	±0.00022
$\overline{uv}/U_{\text{ref}}^2$	±0.000083
$\overline{uw}/U_{\text{ref}}^2$	±0.00013
$\overline{vw}/U_{\text{ref}}^2$	±0.00016
$\overline{u^2 v}/U_{\text{ref}}^3$	±0.000017
$\overline{u^2 w}/U_{\text{ref}}^3$	±0.00002
$\overline{v^2 w}/U_{\text{ref}}^3$	±0.000027
$\overline{uv^2}/U_{\text{ref}}^3$	±0.000015
$\overline{uw^2}/U_{\text{ref}}^3$	±0.000022
$\overline{vw^2}/U_{\text{ref}}^3$	±0.000014
$\overline{uvw}/U_{\text{ref}}^3$	±0.000013
$\overline{u^3}/U_{\text{ref}}^3$	±0.000066
$\overline{v^3}/U_{\text{ref}}^3$	±0.000025
$\overline{w^3}/U_{\text{ref}}^3$	±0.00005

Mean Velocity Results

Figure 11 shows the streamwise mean velocity U/U_{ref} vs y/H for the three bumps. Except for small bump 3, there are much higher U/U_{ref} values near the centerline because of the downwash of the trailing vortices bringing high-velocity fluid down toward the wall while the flow outside the vortex pair is much slower. All profiles of small bump 3, however, have lower U/U_{ref} values for the same y/H than that of the two-dimensional flow. An interesting feature of bump 1 is at $|z|/H < 0.65$. In this region, U/U_{ref} reaches more than $0.55U_{\text{ref}}$ at about $y/H = 10^{-2}$ then decreases to $y/H = 10^{-1}$. Plots of $U^+(= U/U_\tau)$ or $Q^+(= Q/U_\tau)$ vs $y^+(= yU_\tau/\nu)$ profiles using the local U_τ from Fig. 10, which are not presented here, do not collapse onto a single line because there is no law of the wall for mean three-dimensional flows.

Figure 12 shows the spanwise mean velocity W/U_{ref} vs y/H. Bump 1 generates much higher spanwise velocity than bumps 3.

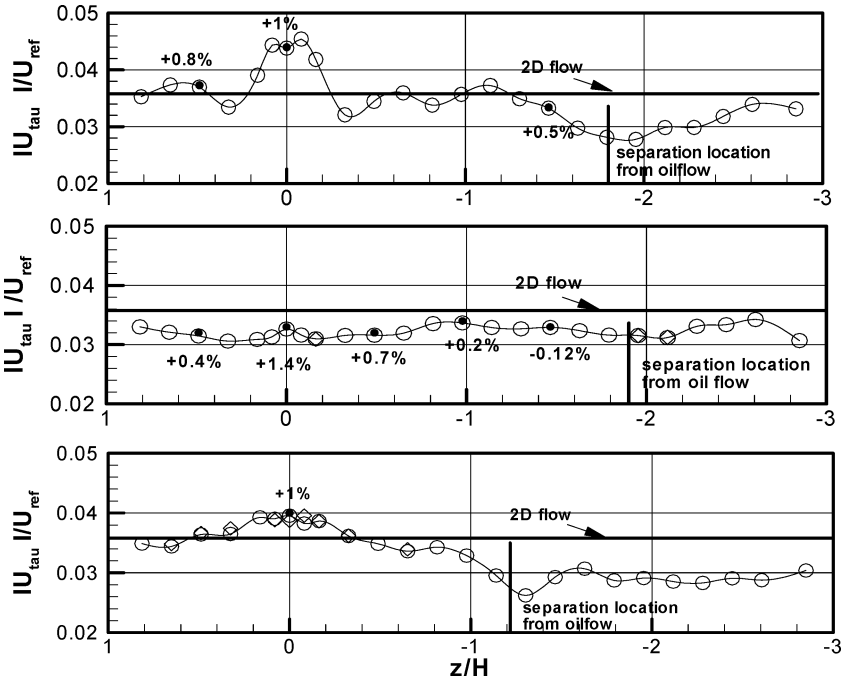

Fig. 10 $|U_\tau|/U_{\text{ref}}$ vs z/H for the three different bumps; top to bottom: large bump 3, small bump 3, and bump 1. (Results from multiple profiles shown as multiple symbols, and filled circles show results with pressure gradient effect.)

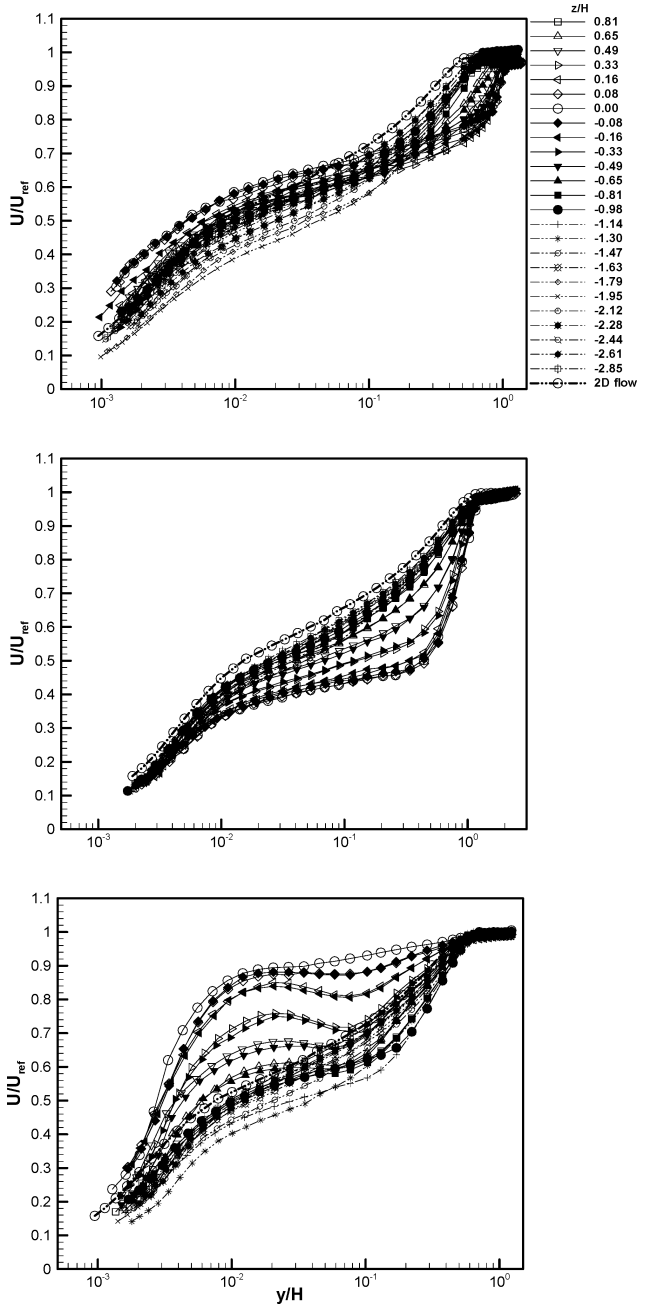

Fig. 11 Streamwise mean velocity profiles in wake plane: large bump 3 at $x/H = 3.63$ (top), small bump 3 at $x/H = 3.26$ (middle), and bump 1 at $x/H = 3.46$ (bottom).

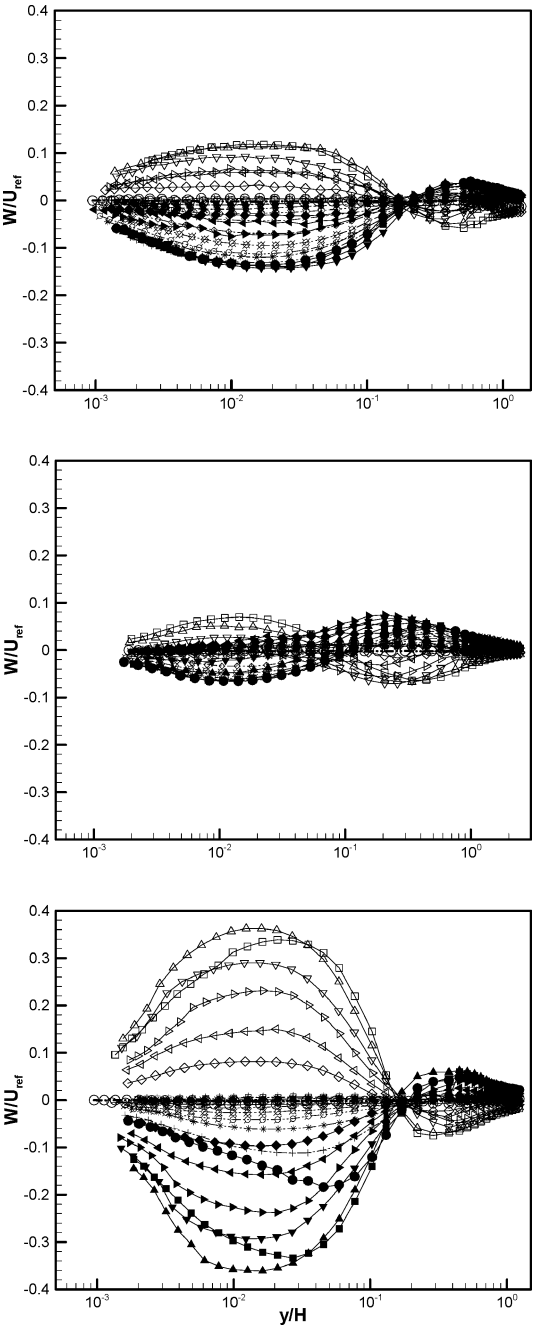

Fig. 12 Spanwise mean velocity profiles in wake plane: large bump 3 (top), small bump 3 (middle), and bump 1 (bottom); z/H as in Fig. 11.

The value of W/U_{ref} is about zero at $y/H \approx 0.2 (y^+ \approx 900)$ for large bump 3 and at $y/H \approx 0.17 (y^+ \approx 700)$ for bump 1, which is the apparent height of the vortex center. In the case of small bump 3, the height of $W/U_{\text{ref}} \approx 0$ is not nearly the same for all z/H and increases away from the center. All bumps reach their maximum W/U_{ref} at $y/H = 10^{-2}$–(2×10^{-2}) for all z/H and show good symmetry about the centerline. In bump 1 there is a relatively huge reduction of W/U_{ref} between $z/H = -0.81$ and 0.98 because the vortex center is at $z/H \approx 0.8$, which is shown clearly in Fig. 13.

Figures 13a and 13b show contours of the mean streamwise U/U_{ref} velocity component and secondary flow velocity component vectors for the three bumps with the linear y/H scale and the $\log_{10}(y/H)$ scale, respectively. The tail of each vector is located at y/H and z/H for that data point. The $\log_{10}(y_0^+)$ scale also was used to show the near-wall region in terms of wall variables and y_0^+, which is the y^+ value based on the two-dimensional flow U_τ. One is able to see the outer-region flow behavior more clearly with the linear scale in Fig. 13a, whereas Fig. 13b magnifies the nearer wall behavior. The contours show the relatively large U/U_{ref} for large bump 3 and bump 1 and the relatively low U/U_{ref} in small bump 3 around the centerline, as shown in Fig. 11. Bump 1 is clearly more effective in bringing high-velocity fluid down toward the wall than the other two bumps. In these plots, there is good apparent symmetry between data on opposite sides of the centerline.

The circulation Γ was calculated for the measurement plane for each bump using a numerical integration along the closed loop around the outer edge of the y–z plane, $0 \le y/H \le 1.23$ and $-2.85 \le z/H \le 0$. It was normalized by U_{ref} and H. Bump 1 has the highest circulation, Γ/HU_{ref} at -0.25. Large bump 3 and small bump 3 have -0.21 and -0.13, respectively.

Figure 14 shows the streamwise vorticity, $\omega_x = (\partial W/\partial y) - (\partial V/\partial z)$, normalized by U_{ref} and H for each bump with the $\log_{10}(y/H)$ and the $\log_{10}(y_0^+)$ scales. Solid lines indicate positive values and dashed lines denote negative values. As expected,

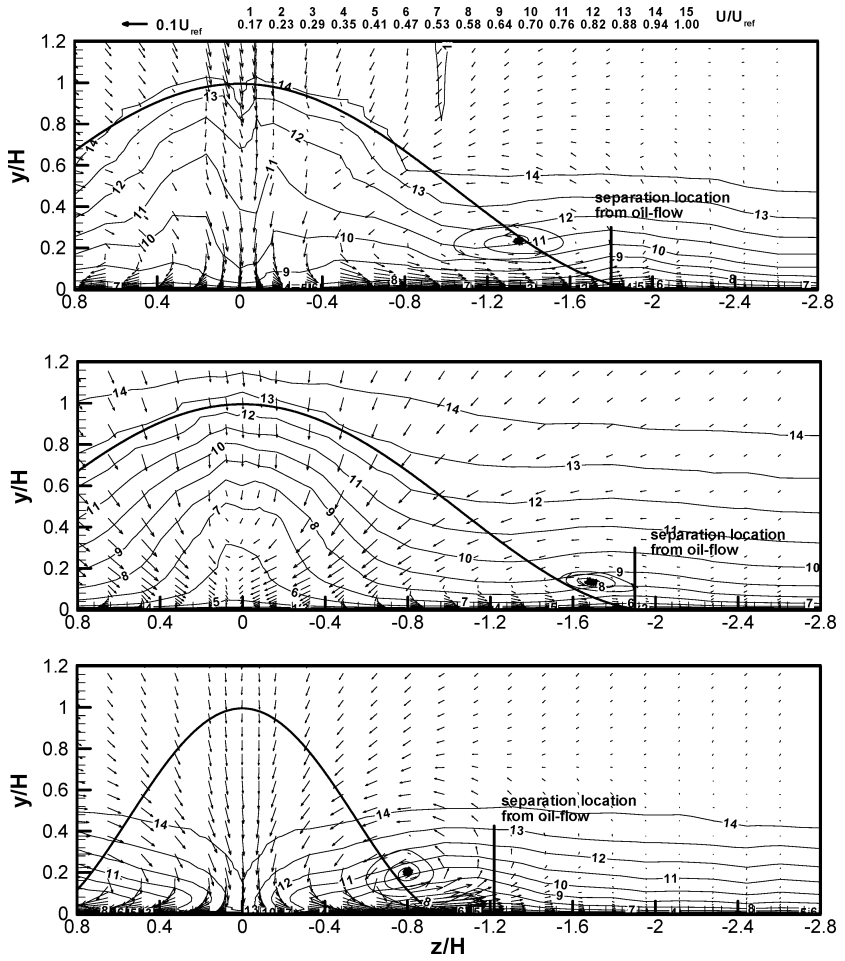

a) Linear y/H scale

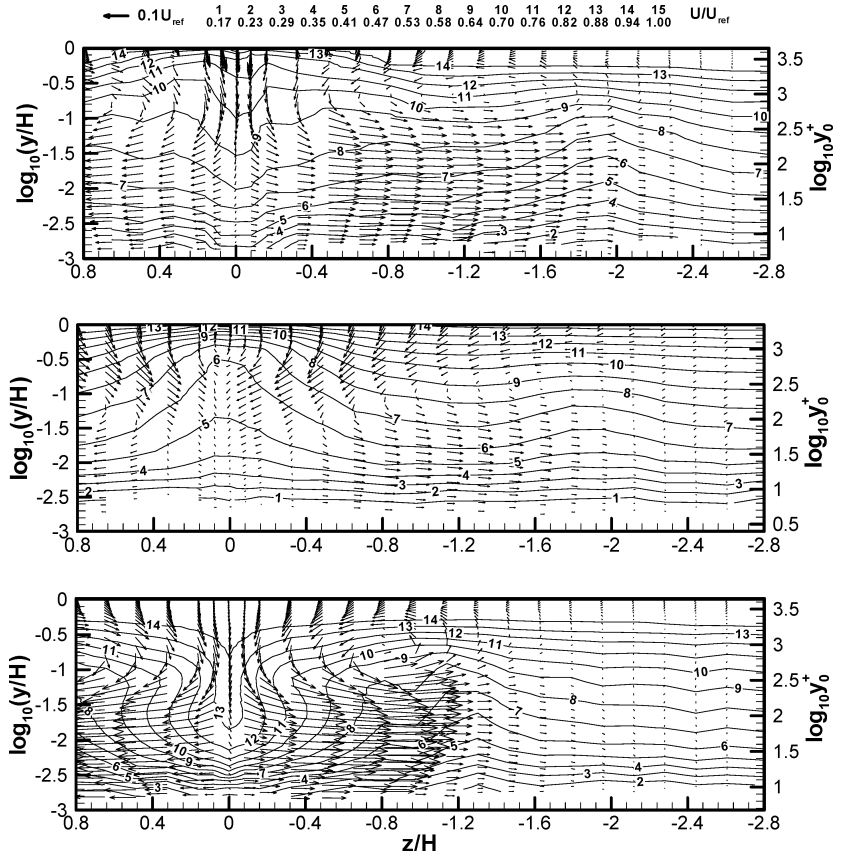

b) Log_{10} (y/H) and $\log_{10}$ (y_0^+) scale

Fig. 13 Mean velocity patterns, U contour and V, W vector: large bump 3 (top), small bump 3 (middle), and bump 1 (bottom).

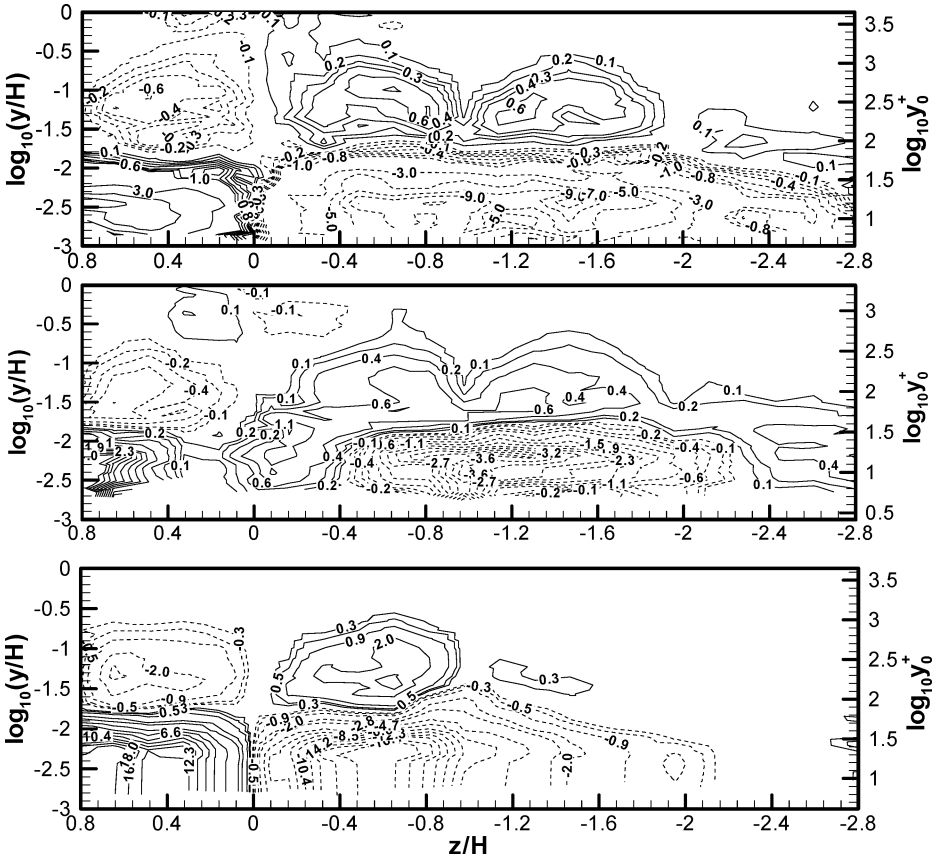

Fig. 14 Contour of normalized streamwise vorticity, $\omega_x H/U_{ref}$, $\log_{10}(y/H)$ and $\log_{10}(y_0^+)$ scale: large bump 3 (top), small bump 3 (middle), and bump 1 (bottom); solid lines are positive values and dashed lines are negative values.

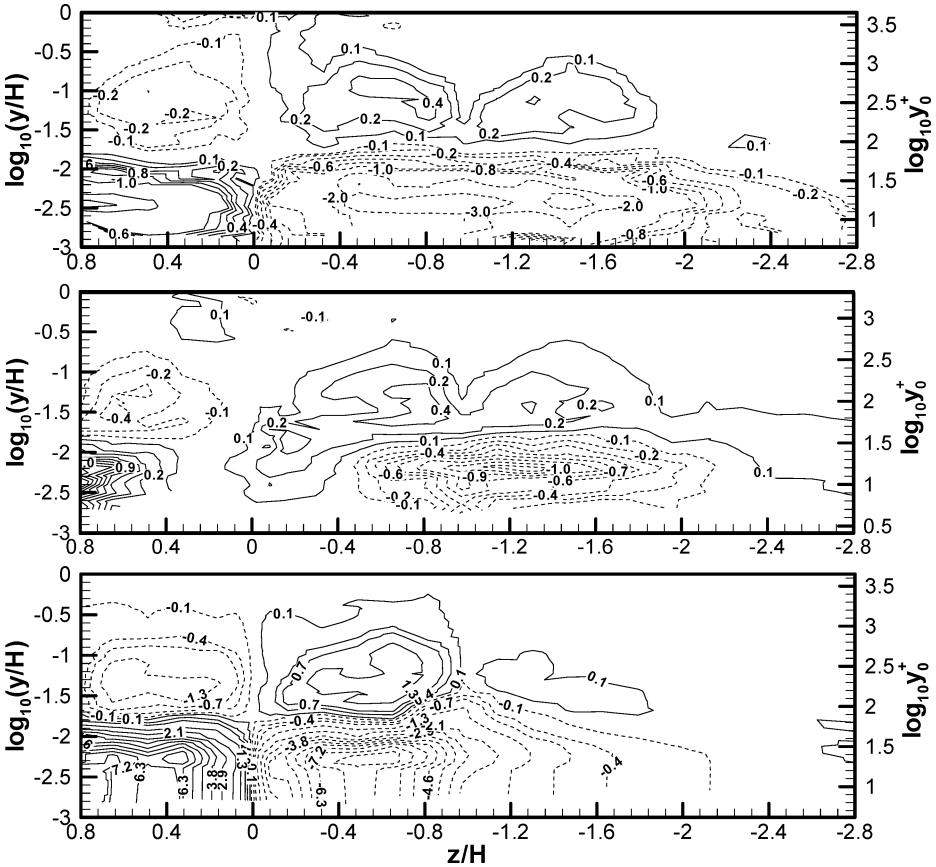

Fig. 15 Contour of normalized helicity density, hH/U_{ref}^2, $\log_{10}(y/H)$ and $\log_{10}(y_0^+)$ scale: large bump 3 (top), small bump 3 (middle), and bump 1 (bottom); solid lines are positive values and dashed lines are negative values.

bump 1 generated the strongest $\omega_x H/U_{\text{ref}}$, having at least two times stronger peak vorticity than the other bumps. The highest $\omega_x H/U_{\text{ref}}$ was generated behind bumps and close to the wall up to $y/H \approx 0.2[\log_{10}(y/H) \approx -0.7]$ due to strong $\partial W/\partial y$ values near the wall (Figs. 12 and 13b). For the $z/H < 0$ region, the contours show the large negative $\omega_x H/U_{\text{ref}}$ near the wall around the streamwise vortex center because of the wall no-slip condition. The sign of $\omega_x H/U_{\text{ref}}$ changed at $y/H \approx 0.02[\log_{10}(y/H) \approx -1.7]$ for all three bumps, because the sign of $\partial W/\partial y$ was changed around that height. For small bump 3, unlike the other two bumps, $\omega_x H/U_{\text{ref}}$ is positive for $-0.4 < z/H < 0$ then negative for $z/H < -0.4$ near the wall. This is because W is still toward the centerline in $-0.4 < z/H < 0$. It is noted that the streamwise vorticity is stronger and more concentrated in bump 1 than in other bumps. This might be related to the spanwise meandering motions for the two bumps 3, which are discussed later.

Figure 15 shows the helicity density, $h = U\omega_x$, normalized by U_{ref} and H for each bump with the $\log_{10}(y/H)$ and $\log_{10}(y_0^+)$ scales. Solid lines indicate positive values and dashed lines denote negative values. For large bump 3 and bump 1, hH/U_{ref}^2 shows distributions similar to those of $\omega_x H/U_{\text{ref}}$ in Fig. 14, indicating higher hH/U_{ref}^2 near the wall, $y/H < 0.03$ $[\log_{10}(y/H) \approx -1.5]$. As for $\omega_x H/U_{\text{ref}}$, bump 1 has a peak hH/U_{ref}^2 that is at least two times larger than that for the other two bumps.

The total helicity, $\mathcal{H} = \iint h \, dy \, dz$, was calculated for the area bounded by the contour used to determine Γ for each bump using

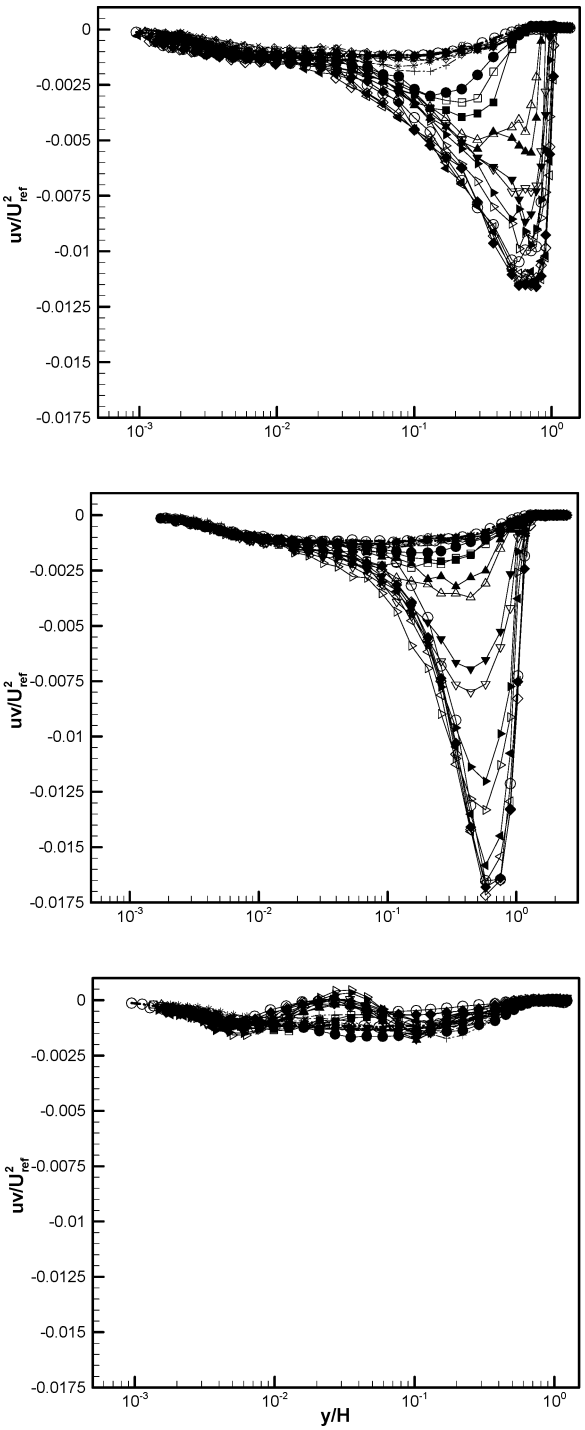

Fig. 16 Streamwise Reynolds shearing stress: large bump 3 (top), small bump 3 (middle), and bump 1 (bottom); z/H as in Fig. 11.

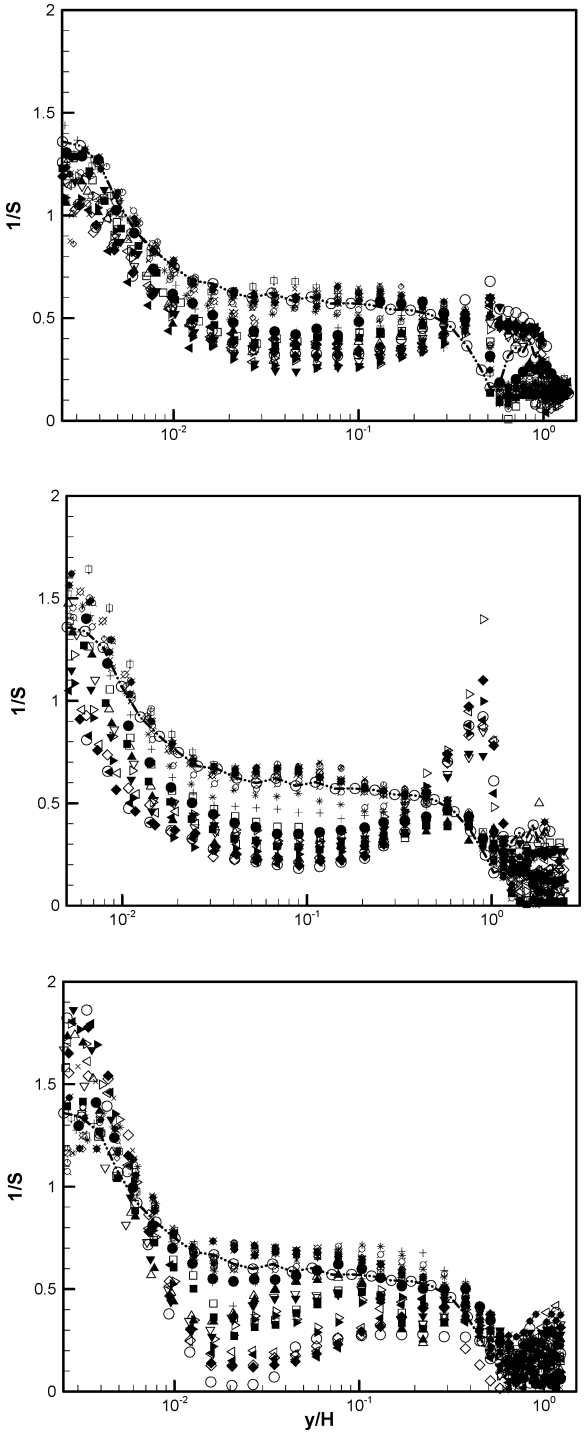

Fig. 17 Parameter 1/S: large bump 3 (top), small bump 3 (middle), and bump 1 (bottom); z/H as in Fig. 11.

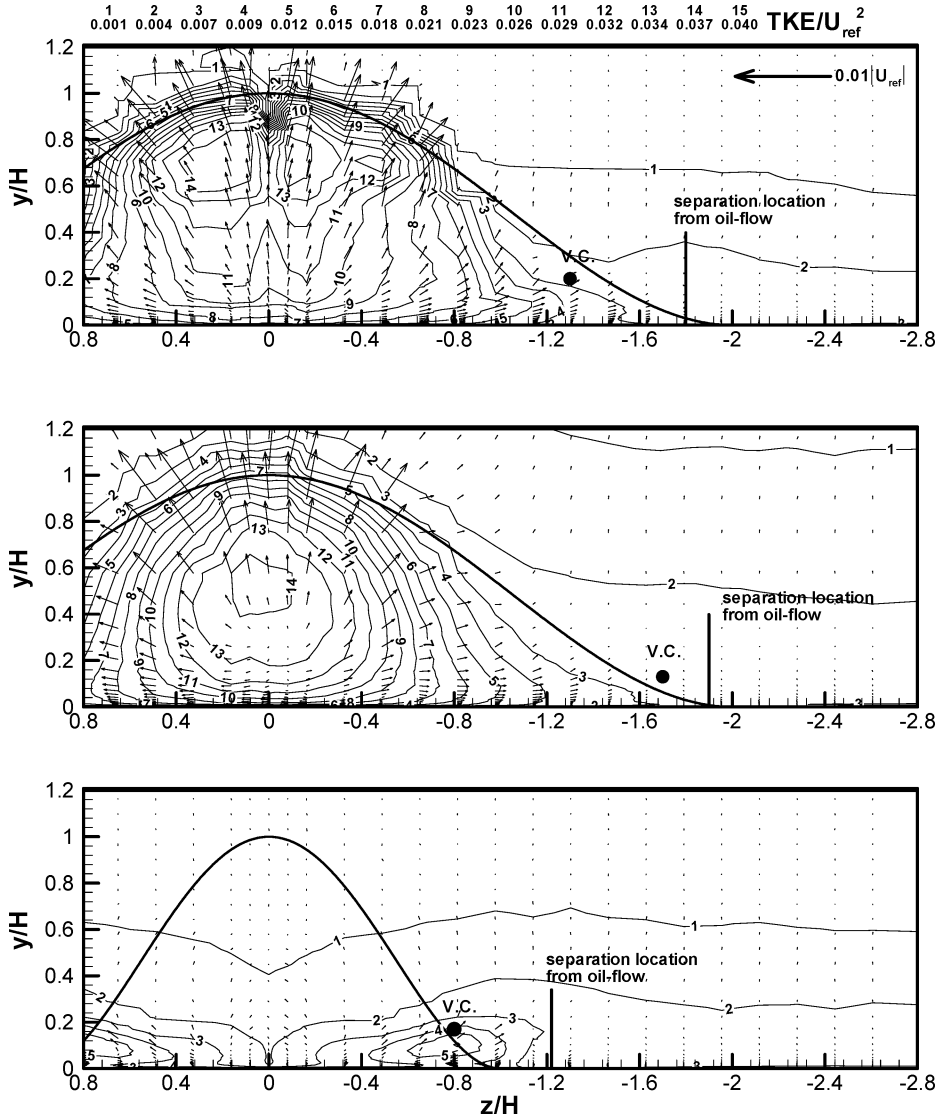

Fig. 18 Contours of TKE and transport velocity vectors: large bump 3 (top), small bump 3 (middle), and bump 1 (bottom); V.C., vortex center.

a numerical integration of the helicity density. It was normalized by U_{ref} and H. Like circulations, bump 1 has the highest helicity, $\mathcal{H}/HU_{\text{ref}}^2$, at 0.22. Large bump 3 and small bump 3 have 0.18 and 0.09, respectively. This means that overall transport of the streamwise vorticity is larger for bump 1 as compared with bumps 3.

Some Reynolds Stress and Triple Product Results

All 6 Reynolds stresses and all 10 triple products were measured for each bump. Only a few results are presented here. Figure 16 shows the streamwise Reynolds shearing stress $-\overline{uv}/U_{\text{ref}}^2$ vs y/H. All bumps have similar profiles up to the height of $y/H \approx 10^{-2}(y^+ \approx 20)$ at all z/H and $|z|/H > 0.98$. When considering $-\overline{uv}$ normalized in wall variables on the local U_τ^2 from Fig. 10, plots of $-\overline{uv}/U_\tau^2$ vs y^+, which are not presented here, show that all profiles collapse better to the height of $y^+ \approx 20$ $(y/H \approx 10^{-2})$ except small bump 3.

In bumps 3 $-\overline{uv}$ it increases as y increases and its maximum values decrease as z/H is farther away from the center. Bump 1 has much lower $-\overline{uv}$ than the other two bumps 3. Generally bump 1 has very low turbulent quantities (not presented here), compared with bumps 3, except for $-\overline{uw}$ and $-\overline{vw}$. This indicates that the spanwise momentum transfer by the velocity fluctuation is higher than the streamwise momentum transfer in bump 1.

The parameter $1/S = [(-\overline{uv})^2 + (-\overline{vw})^2]^{0.5}/v^2$ in Fig. 17 shows some similarities of trends across the flow at almost all z/H locations for each bump. This parameter has been found to have similar behavior for three-dimensional flows as for two-dimensional flows if there are no embedded streamwise vortices.[4] There are embedded streamwise vortices for these three bumps at these locations. Near the wall region bump 1 has higher a $1/S$ value because of higher $-\overline{vw}$ than other bumps. There are two similarities in two z/H regions. For locations farther from the centerline than the mean vortex, the level of $1/S$ up to $y/H < 0.3(y^+ \approx 1000)$ is close to that for the two-dimensional flow and is about the same level as that observed in three-dimensional flows without embedded vortices. Near the centerline where the downwash effects are large, a different similarity is observed.

Figure 18 shows contours of the turbulent kinetic energy, $\text{TKE} = q^2/2 = (u^2 + v^2 + w^2)/2$, and the TKE transport velocity vectors $(V_{qv}\boldsymbol{j} + V_{qw}\boldsymbol{k})/U_{\text{ref}} = vq^2\boldsymbol{j} + wq^2\boldsymbol{k})/q^2U_{\text{ref}}$ derived from the triple products. For bumps 3 away from the wall in the region behind the bump, the large turbulence levels, about 4% of the freestream kinetic energy, are produced by the strong streamwise vortices. However, bump 1 has much lower TKE and has the maximum level just below the vortex center instead behind the bump. Large bump 3 does not show the maximum TKE near the center like small bump 3 because it brings high mean flow momentum more effectively from the freestream. The transport vectors show the large transport of TKE away from where it has the greatest values. The TKE is transported mainly by the w fluctuations near the wall apparently due to the wall damping of the v fluctuations. As the height

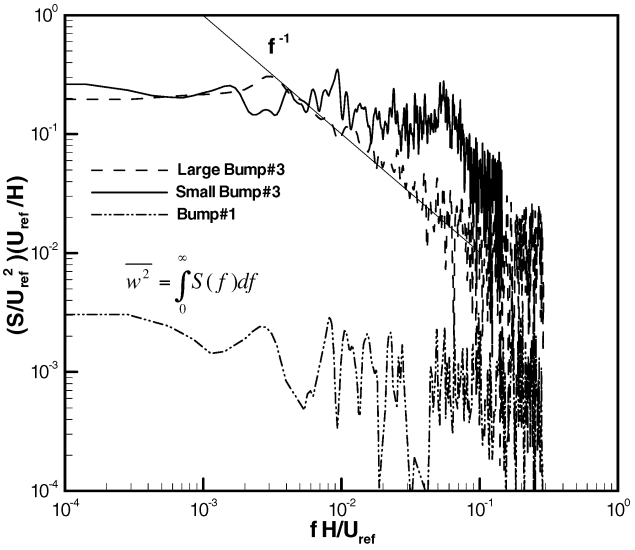

Fig. 19 Normalized w spectra of each bump.

increases the transport by the v fluctuations becomes dominant, especially around the centerline. The region $|z|/H > 1.6$ shows low values of TKE and the transport velocity for each bump.

Some Velocity Spectral Results

To examine the large-scale unsteadiness of the separated flow, a spectrum analysis of the spanwise velocity fluctuation w data at $z/H = 0$ was performed for each bump using a slotting technique.[13] Figure 19 shows the w spectra S normalized by the bump height H and U_{ref} for large bump 3 at $y/H = 0.2$ ($y^+ \approx 900$), small bump 3 at $y/H = 0.12 (y^+ \approx 244)$, and bump 1 at $y/H = 0.17 (y^+ \approx 700)$, respectively, which are at the heights of the mean vortex center of each bump. The maximum $\overline{w^2}$ at the centerline occurred at about the same height. Although the LDV coincident data rate was about 200 Hz, low frequencies with high spectral levels could be examined. For large bump 3 the spectrum has a peak at $fH/U_{\text{ref}} \approx 0.003$ and an f^{-1} slope for $0.003 < fH/U_{\text{ref}} < 0.1$. For small bump 3 the spectrum also has local peaks at $fH/U_{\text{ref}} \approx 0.009$ and 0.05. These results suggest low-frequency large-amplitude spanwise meandering of the large shed vortex structures in bumps 3, such as that suggested by Ishihara et al.[1] and perhaps a large eddy simulation (LES).[14] Small bump 3 shows higher meandering frequency motion and more unsteadiness. Bump 1, however, shows much lower spectrum levels in the entire frequency range. This indicates that the spanwise meandering motion of bump 1 is much weaker than bumps 3. Future data and analysis will examine this unsteadiness further.

Conclusions

Surface mean pressures, oilflow visualizations, and three-velocity-component LDV measurements were presented for turbulent boundary layers over three symmetric bumps. The mean flow appears to be closely symmetric about the centerline for each case. Vortical separations occur on the lee side and merge into two large streamwise vortices downstream.

For the number 3 bumps, at the downstream measurement plane, the near-wall flow is dominated by the wall, whereas the vortices in the outer region produce large turbulence levels near the centerline and appear to have low-frequency motions that contribute to turbulent diffusion. Bump 1, which has a different flow separation pattern showing a relatively sharper separation on the surface from bumps 3, creates a stronger streamwise vortex with very low turbulence levels and more steadiness. Bump 1 is a much more effective vortex generator than bumps 3 for producing higher mean velocity flow near the wall.

The LDV and oilflow results downstream of the bump are clearly consistent with one another. For each bump, the flow along the streamwise centerline is a downwashing reattachment flow with only one mean vortex on each side of the centerline away from the wall.

For large bump 3, the secondary flows are almost the same as the five-hole probe measurement results reported by Willits and Boger[7] for the same-shape bump with the same $\delta/H = \frac{1}{2}$. These two independent sets of results do not support the unpublished computational results for this geometry and flow from several different research groups using several two-equation turbulence models in steady Reynolds-averaged Navier–Stokes (RANS) codes. The k–ω model has been observed to improve calculations for mean two-dimensional separating flows.[8] When used to compute this bump flow, however, a separation is calculated along the centerline and two streamwise mean vortices are produced on each side of the centerline. These current LDV results indicate that this k–ω turbulence model in a steady RANS code does not capture the important physics of this separating vortical three-dimensional flow. The diffusion and merger of the leeside separations into the observed downstream structure need to be better modeled. The low-frequency chaotic meandering of the shed vortex structure for bumps 3 probably needs to be included because this would increase the time-averaged diffusion. Perhaps an unsteady RANS code or LES[14] will capture this unsteadiness. More detailed three-velocity-component LDV measurements closer to the wall and around the locations of the separations are needed for greater understanding and improvements to future models.

Acknowledgments

This work was supported by the U.S. Office of Naval Research under N00014-99-1-0228 (L. P. Purtell and Ron Joslin, Program Managers). The link for tabulated bump data is at http://www.aoe.vt.edu/people/faculty.php?fac_id=rosimpso [cited 14 July 2003].

References

[1]Ishihara, T., Hibi, K., and Oikawa, S., "A Wind Tunnel Study of Turbulent Flow over a Three-Dimensional Steep Hill," *Journal of Wind Engineering and Industrial Aerodynamics*, Vol. 83, 1999, pp. 95–107.

[2]Simpson, R. L., Long, C. H., and Byun, G., "A Study of Vortical Separation from an Axisymmetric Hill," *International Journal of Heat and Fluid Flow*, Vol. 23, 2002, pp. 582–591.

[3]Devenport, W. J., and Simpson, R. L., "Time-Dependent and Time-Averaged Turbulence Structure near the Nose of a Wing-Body Junction," *Journal of Fluid Mechanics*, Vol. 210, 1990, pp. 23–55.

[4]Ölçmen, M. S., and Simpson, R. L., "An Experimental Study of a Three-Dimensional Pressure-Driven Turbulent Boundary Layer," *Journal of Fluid Mechanics*, Vol. 290, 1995, pp. 225–262.

[5]Ölçmen, M. S., and Simpson, R. L., "A 5-Velocity-Component Laser-Doppler Velocimeter for Measurements of a Three-Dimensional Turbulent Boundary Layer," *Measurement Science and Technology*, Vol. 6, 1995, pp. 702–716.

[6]Ölçmen, M. S., Simpson, R. L., and George, J., "Some Reynolds Number Effects on Two- and Three-Dimensional Turbulent Boundary Layers," *Experiments in Fluids*, Vol. 31, 2001, pp. 219–228.

[7]Willits, S. M., and Boger, D. A., "Measured and Predicted Flows Behind a Protuberance Mounted on a Flat Plate," Applied Research Lab. Rept., Penn State Univ., State College, PA, Aug. 1999.

[8]Simpson, R. L., "Aspects of Turbulent Boundary-Layer Separation," *Progress in Aerospace Sciences*, Vol. 32, 1996, pp. 457–521.

[9]Hunt, J. C. R., Abell, C. J., Peterka, J. A., and Woo, H., "Kinematical Studies of the Flows Around Free or Surface-Mounted Obstacles; Applying Topology to Flow Visualization," *Journal of Fluid Mechanics*, Vol. 86, No. 1, 1978, pp. 179–200.

[10]Long, C. H., "A Study of Vortical Separation from Symmetric Bumps," M.S. Thesis, Aerospace and Ocean Engineering, Virginia Polytechnic Inst. and State Univ., Blacksburg, VA (in progress).

[11]Schumann, U., "Realizability of Reynolds Stress Turbulent Model," *Physics of Fluids*, Vol. 20, 1977, pp. 721–725.

[12]Rotta, J. C., "Turbulent Boundary Layers in Incompressible Flow," *Progress in Aerospace Sciences*, Vol. 2, 1962, pp. 70–72.

[13]Roberts, J. B., and Ajmani, D. B. S., "Spectral Analysis of Randomly Sampled Signals Using a Correlation-Based Slotting Technique," *Proceedings of the IEEE*, Vol. 133, 1986, pp. 153–162.

[14]Patel, N., Stone, C., and Menon, S., "Large-Eddy Simulation of Turbulent Flow over an Axisymmetric Hill," AIAA Paper 2003-0967, Jan. 2003.

H. Reed
Associate Editor